Dynamical and Physical Processes Associated with Orographic Precipitation in a Conditionally Unstable Uniform Flow: Variation in Basic Wind Speed

GÖKHAN SEVER

Department of Energy and Environmental Systems, North Carolina Agricultural and Technical State University, Greensboro, North Carolina, and Environmental Science Division, Argonne National Laboratory, Argonne, Illinois

YUH-LANG LIN

Department of Physics, and Department of Energy and Environmental Systems, North Carolina Agricultural and Technical State University, Greensboro, North Carolina

(Manuscript received 8 March 2016, in final form 8 November 2016)

ABSTRACT

A series of systematic two- and three-dimensional (2D and 3D, respectively) idealized numerical experiments were conducted to investigate the combined effects of dynamical and physical processes on orographic precipitation with varying incoming basic-flow speed U in a conditionally unstable uniform flow. In addition to the three moist flow regimes found in Chu and Lin at lower wind speeds, a new flow regime, regime IV, is found for higher wind speeds ($U > 36\,\mathrm{m\,s^{-1}}$) and is characterized by gravity waves and heavy precipitation and lack of upper-level wave breaking and turbulence over the lee slope. The transition from regime III to regime IV at $36\,\mathrm{m\,s^{-1}}$ is explained by the transition from upward-propagating gravity waves to evanescent flow, which can be predicted with a modified mountain wave theory. Although the basic features are captured well in low grid resolution ($\Delta x = 1$ km), high-resolution ($\Delta x = 100$ m) 2D and 3D simulations are required to resolve precipitation distribution and intensity at higher basic winds ($U > 30\,\mathrm{m\,s^{-1}}$). Based on 3D simulations, gravity wave–induced severe downslope winds and turbulent mixing within hydraulic jump reduce orographic precipitation in regime III. A preliminary budget analysis indicated that, in regime IV, orographic precipitation further increases as a result of enhanced rain processes when the blocking effect of wave breaking vanishes.

1. Introduction

When tropical cyclones impinge on mesoscale mountains, such as the Appalachians in the United States, the mountainous islands of the Caribbean Sea, La Réunion and the Madagascar islands of the Indian Ocean, and the Central Mountain Range (CMR) of Taiwan, many of them [e.g., Hurricane Ivan (2004), Hurricane Jeanne (2004), Tropical Cyclone Gamede (2007), Typhoon Morakot (2009), respectively] result in heavy precipitation. The devastating property damage and loss of lives resulting from flash flooding and debris flow associated with extreme orographic rain events demand more study of their enhancement and/or generation mechanisms. Although isolated islands have served as the subject of many orographic rain studies, robust quantitative precipitation forecast (QPF) over longer mountain ranges remains a challenge to the forecast community.

Recent studies of orographic effects on precipitating systems have shown that orographic precipitation involves complicated microphysical and dynamical interactions (Houze 2012), which may play major roles in the enhancement and suppression of orographic precipitation. For example, the following processes have been found in previous studies: "(a) increase of upward transport of water vapor and hydrometeors as mountain height increases; (b) enhancing the accretion processes through forced lifting and the reduction of the lifting condensation level over the mountain surface as mountain height increases; (c) changes in microphysical pathways in the production of precipitation; (d) interception of hydrometeors by a mountain surface at a higher level; (e) changes in the horizontal advection scale of air motion compared to the time scale for

Corresponding author e-mail: Yuh-Lang Lin, ylin@ncat.edu

DOI: 10.1175/JAS-D-16-0077.1

microphysical process; (f) changes in precipitation efficiency; (g) enhanced evaporation over the downslope with the addition of adiabatic warming; and (h) small-scale heavy orographic precipitation via turbulent motion'' (Lin 2007, p. 475). Part of the forecasting problem is due to a lack of understanding of the interactions among dynamical, thermodynamical, and microphysical processes and their impact on orographic rain generation or enhancement. Some of these dynamical and physical processes will be explored in this study.

Most of the studies on orographic precipitation formation, enhancement, and evolution that are associated with orographic forcing and atmospheric instabilities are limited to relatively lower wind regimes. To improve the understanding of the problem, one approach is to make idealized simulations with mesoscale numerical models. Idealized simulations of the formation and evolution of orographic precipitation have been actively studied in the past several decades (e.g., Chu and Lin 2000, hereafter CL00; Colle 2004; Chen and Lin 2005a,b; Chen et al. 2008; Miglietta and Rotunno 2009, hereafter MR09; Miglietta and Rotunno 2010, 2014). Some of these studies have used different mesoscale models to study orographic precipitation under idealized upstream conditions for a conditionally unstable flow passing over an idealized bell-shaped mountain. These studies showed that mountains may enhance as well as induce precipitation through the interactions of dynamical, microphysical, and thermodynamical processes associated with the impinging airstreams. In this study, our major interest is the heavy orographic precipitation induced and/or enhanced by orography during tropical cyclone (TC) passage over a mesoscale mountain. This scenario often provides favorable conditions for heavy precipitation. However, the dynamics for this extremely large Froude number flow is still not well explored.

Based on idealized simulations using the Advanced Regional Prediction System (ARPS) (Xue et al. 2000), CL00 identified three moist flow regimes for a conditionally unstable flow over an idealized two-dimensional (2D) mesoscale mountain: (i) an upstream-propagating convective precipitation system, (ii) a quasi-stationary convective system over the mountain, and (iii) a quasi-stationary convective system in the vicinity of the mountain peak along with downstream-propagating convective system. The evolution of regime I is explained by convectively triggered cells upstream of the mountain due to an upstream-propagating density current formed by evaporative cooling process. In regime II, a force balance between orographic forcing and cold-air outflow plays a role in the quasi-steady precipitation concentrated over the mountain. Orographic forcing is the key driving force for the quasi-stationary precipitation in regime III, as well as in the earlier regimes. Propagating precipitation is caused by convection triggered ahead of the hydraulic jump over the lee slope and is advected by the basic flow. These regimes were classified based on the magnitude of upstream unsaturated moist Froude number ($F_w = U/N_w h$). Here, U is the basic-flow speed, h is the mountain height, and N_w is the unsaturated moist Brunt–Väisälä frequency (e.g., Chen and Lin 2005b). Note that it can be derived that $U/N_w h$ in a stratified fluid flow is equivalent to the ratio of kinetic and potential energy changes in a stratified fluid over topography, as defined in the shallow-water system ($U/\sqrt{gH}$) (Sun and Sun 2015). Thus, in this study, we prefer to use the Froude number, instead of nondimensional mountain height as defined as Nh/U (Baines 1995). In the current study, CL00 is revisited to explore new dynamics and physics, especially under a much wider range of basic-flow speed.

Chen and Lin (2005b) extended CL00 to include the convective available potential energy (CAPE), in addition to F_w. Based on F_w and CAPE, Chen and Lin identify four flow regimes for a conditionally unstable flow over an idealized 2D mountain, in which the flow characteristics are explained by the interplay among orographic blocking, advection, and density current forcing. It was found that under low-CAPE flows, orographic precipitation can be modulated by large horizontal wind speeds. The implication of this finding for a tropical cyclone is that the precipitating system does not necessarily require high CAPE to produce heavy orographic rainfall (Huang and Lin 2014). However, different combinations of CAPE and U lead to different precipitation types. CL00 study has also been extended to 3D by Chen and Lin (2005a), but with 3D mountain geometry; thus, it cannot be used for direct comparison. The four moist flow regimes proposed in Chen and Lin (2005b) were further extended by Chen et al. (2008) to include F_w and h/a (mountain aspect ratio, with a the mountain half-width). MR09 performed a series of conditionally unstable flows impinging on a mesoscale mountain ridge on a three-dimensional domain and at high resolution ($\Delta x = 250$ m) to properly resolve cellular-scale features. Basically, the overall flow characteristics are similar to those found in CL00. In addition, they proposed a functional dependence of the rain rate on three parameters, related respectively to the triggering and the orographic forcing of convection and to the ratio of the advective to convective time scales. MR09 is extended to cover larger regions of the parameter space, including experiments corresponding to a wider range of CAPE (Miglietta and Rotunno 2010). It is found here that the low-CAPE, moderate-wind experiments do not fit the functional dependence

for rain rate amount and location proposed in MR09. The analysis of Miglietta and Rotunno (2010) suggested that two additional nondimensional parameters should be taken into account. While this series of studies on flow regimes of conditionally unstable flow over mesoscale mountains has significantly improved our understanding of dynamical and physical processes associated with orographic precipitation, our understanding of flow and precipitations in higher wind regimes is still limited. In this study, we will extend the study of CL00 to higher wind so that the results can be applied to orographic precipitation induced during the passage of TCs over mesoscale mountains.

Although previous studies (CL00, MR09, among others) have investigated the impact of dimensionality and sensitivity on convection and orographic precipitation, connection between different simulation setups are not well documented, especially across a large range of wind speeds. We aim to bridge the gap of simulation sensitivities by considering a wind speed range from 1 to 50 m s^{-1} using a moderately-large-CAPE (1900 J kg^{-1}) flow over a fixed bell-shaped mountain. This research follows the approach taken by CL00, which relies on studying the basic control parameters that affect orographic flow and precipitation in a conditionally unstable flow using idealized, low-resolution 2D simulations as well as high-resolution 2D and 3D simulations. Basic-flow speed variations within 1–50 m s^{-1} are used for low-resolution simulations, while keeping other model settings and sounding parameters unchanged, including wind variation with height. A few selected high-resolution 3D simulations are performed to investigate precipitation formation and evolution, particularly at high wind speeds. The following research questions are addressed: (i) How do flow characteristics vary in 2D and 3D simulations and low- and high-grid resolutions? (ii) What are the moist flow regimes and their orographic precipitation characteristics under a wide range of basic wind speeds (say, 1–50 m s^{-1}), especially under high-wind regimes? (iii) What determines critical wind speeds for flow regime boundaries? (iv) How are the distributions and evolutions of hydrometeors?

The rest of the paper is organized as follows. In section 2, the numerical experimental design used in this study will be described. The structural evolution of flow regimes will be discussed in section 3. This discussion includes a reproduction of previous studies using a different model as well as key differences in the setup. A theoretical analysis is provided to explain the flow dynamics at very high wind speeds, which is a part of the parameter space that was not considered previously. Section 4 is devoted to the explanation of how the low- and high-resolution 2D and 3D simulations performed throughout the low- to high-wind-speed conditions. After highlighting the simulation characteristics and documenting the limitations of 2D simulations, flow dynamics and physics analyses in strong flow will be provided in section 5 using high-resolution 3D simulations. Concluding remarks can be found in section 6.

2. Numerical experimental design

This research employs the CM1 (release 17) (Bryan and Fritsch 2002) for the numerical simulations. A set of low- and high-resolution 2D and 3D simulations are performed. Most of the simulation settings are the same in these experiments, except the domain geometry setup and a few numerical options. A free-slip boundary condition is applied at the bottom boundary. The 1.5-order turbulent kinetic energy (TKE) closure is chosen for subgrid turbulence scheme. Rotational effects are ignored by setting the Coriolis parameter to zero. Planetary boundary layer (PBL) and radiation parameterizations are deactivated for all simulations, similar to CL00's idealized simulations. The Goddard Lin–Farley–Orville (Lin et al. 1983; Tao and Simpson 1993) microphysics parameterization scheme (single moment) is used to explicitly resolve microphysical processes and precipitation. No perturbation is added to either on mountain profile or initial sounding variables. Without adding small-amplitude perturbations to initiate convective cells at the initial time, the y asymmetry of turbulent eddies will be developed associated with orographic forcing through the triggering of conditional instability, for example.

Turbulence is readily triggered once the convection is initiated in simulations. Each simulation is run for 12 h and the simulated fields are output at every hour. The Runge–Kutta third-order time integration method is applied to advance the model forward in time.

A 2D bell-shaped mountain represents the idealized terrain. The mountain profile is identical to CL00 and is described by the following equation:

$$h(x) = \frac{h}{(x/a)^2 + 1}, \tag{1}$$

where h and a are the mountain height and half-width, respectively. They are fixed as 2 and 30 km, respectively, in all simulations. Particular details of simulation setups are provided in the following subsections.

a. 2D low-resolution simulations

A fifth-order advection scheme is employed both for horizontal and vertical scalars and velocities. The horizontal grid spacing is 1 km in x direction Δx. The vertical grid spacing Δz is 250 m from the surface to 9 km, stretched to 500 m from 9–10.5 km, and then stays as

constant up to the domain top at 20 km, similar to the setup used in MR09. A sponge layer is added from 14 km to the domain top to absorb wave energy generated in the physical domain. The total grid points of the domain in the x and z directions are 1000×59. The model time step Δt is 1 s. West–east lateral boundaries are chosen to be open so that the disturbances generated within the domain can propagate out. These simulations are referred as 2D-Low for brevity. Moist flow regime categorization is made based on the fine wind speed increment ($1\,m\,s^{-1}$) simulations in the range of 1–50 $m\,s^{-1}$. The same vertical and horizontal turbulence coefficients are specified in these simulations for the turbulence scheme. Later analyses use 2D simulations with different spatial turbulence coefficients. This change introduces only a small variation in the precipitation intensity, for the sake of consistency, a few selected 2D-Low experiments are repeated with the latter turbulence configuration.

b. 2D and 3D high-resolution simulations

High-resolution 2D simulations employed the same fifth-order scheme for advection of the fields. To maintain the stability of 3D high-resolution simulations, a sixth-order scheme is employed with sixth-order artificial diffusion applied to all prognostic variables. A high-resolution horizontal grid spacing of 100 m is specified within $x = [-100, 100]$ km, then stretched it to 1 km at the end of the domain boundaries at ±500 km. The y-domain width for 3D simulations is 10 km, which is mainly chosen to resolve 3D characteristics of convective precipitation within a reasonable simulation time. Sensitivity studies performed with larger domain widths show similar flow and precipitation behaviors. The grid spacing is 100 m and no grid stretching is applied in the meridional extent. A vertical grid spacing of 100 m is applied from the surface to 6 km, which is then stretched to 500 m up to 12 km and fixed until the domain top at 20 km. The same bell-shaped profile is employed in 3D simulations, which is essentially a 2D bell-shaped mountain uniformly extended in the y direction to make it a 3D mountain. Adaptive time stepping with an initial value of 1 s is used for the integration. These simulations are referred to as 2D-High and 3D-LES for brevity. Following the resolution requirements of MR09 (<250 m) and Schalkwijk et al. (2015) (~100 m), the vertical and horizontal resolutions employed in the high-resolution setup are assumed to be able to simulate turbulent flow over the idealized terrain.

c. Idealized sounding

Figure 1 shows the idealized, conditionally unstable Weisman and Klemp (1982) sounding that is used to initialize the simulations. Its analytical expressions can be found in the original paper and in CL00. Several important properties of this sounding are 1) the westerly wind profile is uniform throughout the vertical domain; 2) CAPE is about $1900\,J\,kg^{-1}$ and the equilibrium level (EL) extends up to near the tropopause (11.5 km), which is favorable for production of deep convective cells; 3) the lifting condensation level (LCL) is at about 1 km and the level of free convection (LFC) is at 1.6 km (note that the LFC is below the 2-km mountain height, which means the mountain can mechanically trigger conditional instabilities); and 4) the surface air temperature is near 27°C, the freezing level is located at near 3.5 km, and $14\,g\,kg^{-1}$ of water vapor is available up to slightly above the LCL. The sounding parameters are calculated using the getcape.F script provided in the CM1 based on the surface parcel ascent. The most unstable parcel and mixed-layer (lowest 500 m) parcel options yield CAPE values of about 2300 and $1950\,J\,kg^{-1}$, respectively.

3. Moist flow regimes and their relevant dynamics

a. Moist flow regimes in 2D low-resolution simulations

Some key flow dynamics and precipitation characteristics within the range of 1–50 $m\,s^{-1}$ are provided to demonstrate the current model is able to reproduce previous moist flow regimes to better highlight the simulation differences in the next section. Based on the 2D-Low simulations (Fig. 2), we identify four regimes for a uniform, conditionally unstable flow over a bell-shaped mountain:

1) Regime I (U = 1–7 $m\,s^{-1}$): this regime is characterized by an upstream-propagating precipitating system with light convective precipitation over the mountain.
2) Regime II (U = 7–9 $m\,s^{-1}$): this regime is characterized by stationary and heavy convective precipitation over the mountain.
3) Regime III (U = 9–36 $m\,s^{-1}$): this regime is characterized by deep convection over the upslope and hydraulic jump and severe downslope winds over the downslope.
4) Regime IV ($U > 36\,m\,s^{-1}$): this regime is characterized by strong deep convection and turbulence over upslope and in the vicinity of the mountain peak, with gravity waves and heavy precipitation over the lee slope.

In this scenario, orographic precipitation is mainly driven by stationary and propagating forcings. The stationary forcing persists throughout the regimes as it is initiated by a steady supply of flow and a fixed mountain.

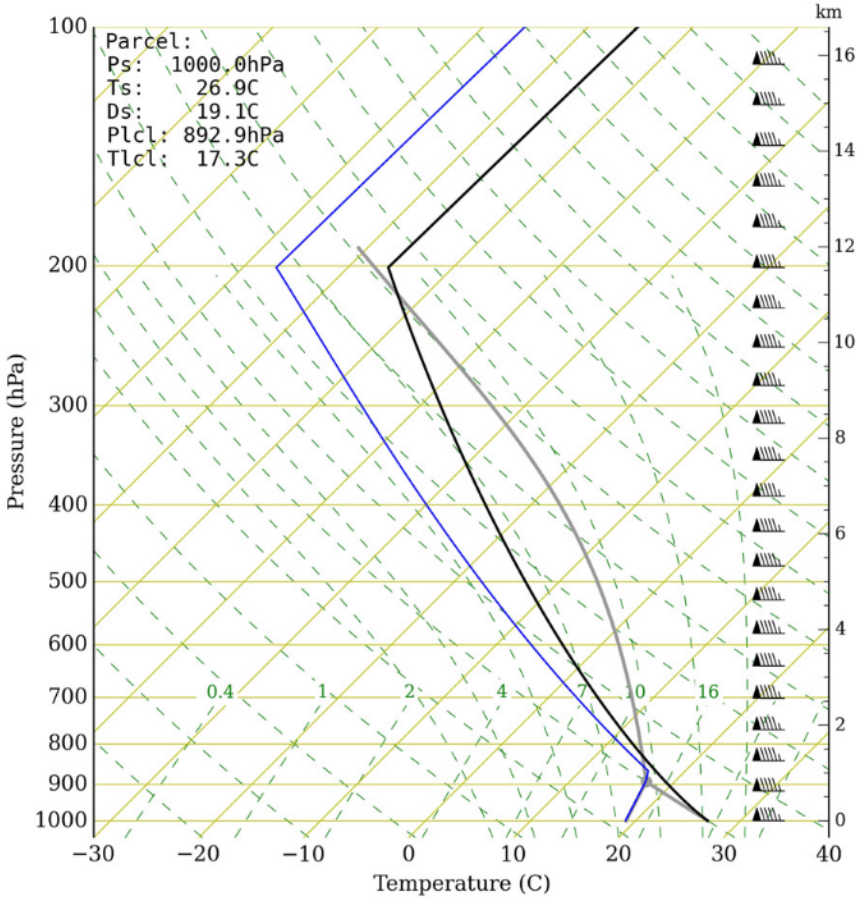

FIG. 1. Skew T diagram of the Weisman and Klemp (1982) sounding used for all the simulations. Note that the wind profile is representative for $U = 47.5\,\mathrm{m\,s^{-1}}$.

Then the propagating forcing is provided by an evaporative cooling–induced density current at low wind speeds, which pushes the precipitation upstream of the mountain. Once the wind speed is in the regime II and early regime III range, advective forcing causes downstream movement of the precipitation. Although the first three regimes classified in this study are similar to those found in CL00, there are significant differences in regime boundaries, flow, convection, and precipitation characteristics. First, the transitional regime (regime II) occurs at $U = 7$–$9\,\mathrm{m\,s^{-1}}$, instead of at around $U = 4\,\mathrm{m\,s^{-1}}$ in CL00, which appears to be caused by differences in model numerics, physical parameterization schemes, and detailed experimental settings. Second, at the higher wind range, part of the precipitating system, while still producing heavy convective rainfall up to $U = 15\,\mathrm{m\,s^{-1}}$, is advected away from the mountain and induces complicated microphysical and dynamical interactions. Third, a new regime (regime IV) is classified as a result of having a significantly different precipitation pattern than regime III when $U > 36\,\mathrm{m\,s^{-1}}$, which is equivalent to a category-2–3 hurricane wind, which was not considered in CL00. In this flow regime, upper-level wave breaking vanishes and a heavier precipitation region retreats to near the mountain peak.

The basic-flow and precipitation parameters for higher-flow regimes (III and IV) are summarized in Table 1. Among the cases, the maximum rainfall rate $R_{\max}$ is largest when $U = 10\,\mathrm{m\,s^{-1}}$ and smallest when $U = 20\,\mathrm{m\,s^{-1}}$. Although the orographic lifting is relatively weak in regime III, strong updrafts are generated when a relatively large CAPE in the incoming flow is released as low-level air parcels are lifted by the mountain beyond their LFCs. In terms of total precipitation maximum $R_{t\max}$, lower winds in regime III shows large accumulations, which is in agreement with one of the heavy precipitation ingredients (slow movement of the convective system) described in Lin et al. (2001, p. 652). However, the total precipitation responds differently to the change in U with different simulation setups. High-resolution simulations show an increasing trend in total precipitation, whereas the trend in low-resolution cases is not consistent.

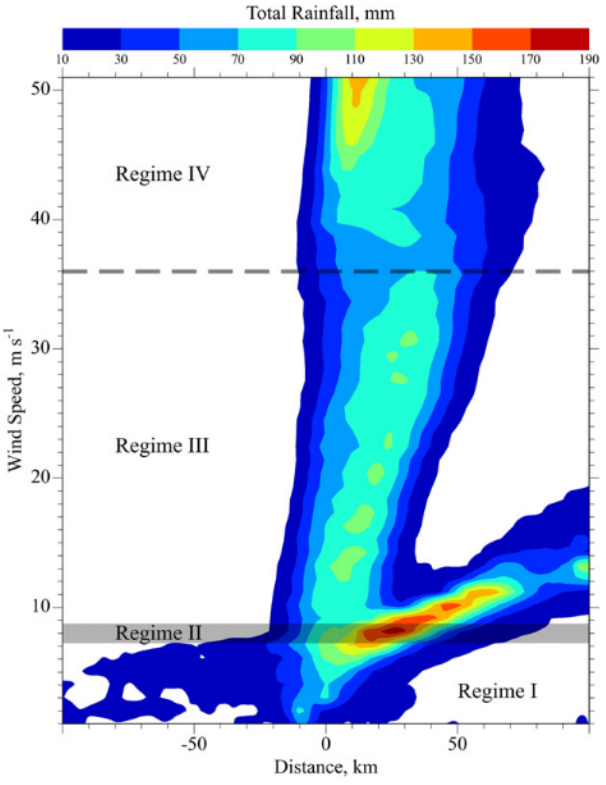

FIG. 2. Distributions of 12-h accumulated rainfall distribution based on fine-increment 2D-Low simulations. The plotting domain only shows part of the simulated total domain [−100, 100] km. Flow regime boundaries are denoted with dashed lines or shading. Regime I, II, III, and IV are approximately classified as U = (1, 7), (7, 9), (9, 36), and >36 m s^{-1}, respectively.

With limited sensitivity experiments at this stage in the research, we have found the moist flow regimes can be approximately classified using this set of 2D low-resolution simulations. However, there are differences in flow behavior and the evolution of orographic precipitation at finer resolution (dx = 100 m) and in 3D. Some key differences in simulation results and the justifications for studying high-resolution 2D and 3D simulations will be discussed in section 4.

b. *Theoretical basis for flow transition*

Applying the dry mountain wave theory (e.g., Smith 1979; Lin and Wang 1996; Lin 2007) to a quasi-steady, linear moist flow near the mountain, the Scorer's equation for a dry flow over 2D isolated mountains in the Fourier or wavenumber space may be extended to a moist flow [Barcilon et al. 1979; see Lin (2007), section 5.2, "Flows over two-dimensional isolated mountains," for a brief review]:

$$\frac{d^2\hat{w}}{dz^2} + (l_w^2 - k^2)\hat{w} = 0, \tag{2}$$

where $\hat{w}$ is the vertical velocity, l_w is the moist Scorer parameter defined as $\sqrt{N_w^2/U^2}$ for a uniform flow, N_w is the unsaturated moist Brunt–Väisälä frequency [$\sqrt{(g/\theta_v)(\partial\theta_v/\partial z)}$, where θ_v is the virtual potential temperature for the unsaturated moist air], and k is the terrain wavenumber ($2\pi/a$). Since the general flow dynamics is driven by the upstream profile of the atmosphere, employing an unsaturated profile of N is a reasonable assumption. In addition, it is assumed that moist profiles, which are associated with convection and precipitation, have local nonlinear effects, considering that these effects are stationary near the mountain under high-wind conditions. Note that in (2), the diabatic heating associated with the latent heat is assumed to be proportional to the vertical velocity and absorbed into the unsaturated Brunt–Väisälä frequency on the left side of the equation. For a constant Scorer parameter, the solution can be obtained in the following form:

TABLE 1. Summary of the basic-flow and precipitation parameters for select 2D-Low, 2D-High, and 3D-LES setups. Basic-flow speed U, unsaturated moist Froude number F_w, unsaturated moist Brunt–Väisälä frequency N_w is assumed as 0.0075 s^{-1}, and estimated orographic lifting w_{oro} (with maximum mountain slope = 0.043), maximum rain rate R_{max}, maximum total rainfall R_{tmax}, and location of maximum total rainfall X_{tmax} are listed. The horizontal resolutions of the setups are 1 km for 2D-Low and 0.1 km for 2D-High and 3D-LES.

U (m s^{-1})	Flow regime	F_w (U/N_wh)	$w_{oro} \approx U\partial h/\partial x$ (m s^{-1})	Setup	R_{max} (mm h^{-1})	R_{tmax} (mm)	X_{tmax} (km)
10	III	0.67	0.43	2D-Low	19.4	132.3	49.5
				2D-High	18.3	90.8	34.6
				3D-LES	19.3	119.9	62.9
20	III	1.33	0.86	2D-Low	14.1	106.6	−0.5
				2D-High	12.3	119.4	2.8
				3D-LES	10.0	97.3	2.2
30	III	2.0	1.29	2D-Low	15.4	119.4	28.5
				2D-High	14.1	141.5	8.2
				3D-LES	13.7	128.6	7.5
40	IV	2.67	1.72	2D-Low	14.4	110.3	4.5
				2D-High	18.2	182.4	5.8
				3D-LES	16.9	176.3	10.9

$$\hat{w}(k,z) = \hat{w}(k,0)e^{i\sqrt{l_w^2-k^2}z} \quad \text{for} \quad l_w^2 > k^2 \quad \text{and} \tag{3a}$$

$$\hat{w}(k,z) = \hat{w}(k,0)e^{-\sqrt{k^2-l_w^2}z} \quad \text{for} \quad l_w^2 < k^2. \tag{3b}$$

The magnitude comparisons of l_w and k provide a critical regime boundary for vertically propagating gravity waves when $l_w > k$ and evanescent waves when $l_w < k$.

From the sounding of Fig. 1, N_w can be estimated as $75 \times 10^{-4}\,\mathrm{s}^{-1}$ (0.0075) at the surface and 1 km. Using the mountain width of 30 km, k is $2.1 \times 10^{-4}\,\mathrm{m}^{-1}$. Then corresponding values of l_w are 7.5×10^{-4}, 3.75×10^{-4}, 2.5×10^{-4}, and $1.88 \times 10^{-4}\,\mathrm{m}^{-1}$ for cases U10, U20, U30, and U40, respectively. Therefore, an evanescent flow behavior is expected at $U = 40\,\mathrm{m\,s}^{-1}$, which is how the simulated flow behaves. From this comparison, it is expected to see a flow regime transition at $U = 36\,\mathrm{m\,s}^{-1}$. The 2D-Low simulations with finer U increments confirm that the flow regime transition does occur at $U = 36\,\mathrm{m\,s}^{-1}$. By comparison, our dry flow simulations show this transition occurs at $U = 40\,\mathrm{m\,s}^{-1}$, which is $4\,\mathrm{m\,s}^{-1}$ greater than that for the moist flow (not shown). This difference highlights the impact of moisture on stability and, particularly, the roles of warming associated with latent heat and hydrometeor drag.

4. Sensitivities to resolution and dimensionality

There are some substantial differences in basic-flow dynamics, physics, and precipitation structure among low-resolution 2D and high-resolution 2D and 3D simulations. Before high-wind simulations are investigated, some analyses are carried out to demonstrate resolution and dimensionality issues since they might impact the reliability of these simulated results. With the increasing availability of computational resources, high-resolution 3D simulations are favored for simulating turbulent flows and convective precipitation. However, 2D low-resolution simulations are still commonly adopted for their ease of use and for providing a feasible benchmark test bed for idealized simulations. In an attempt to reproduce the findings of CL00 and MR09, we ran a set of 2D low-resolution (2D-Low), 2D high-resolution, and 3D high-resolution simulations. Since the horizontal and vertical resolutions used in high-resolution 2D and 3D simulations are in the range of LES, these simulations are called 2D-High and 3D-LES, respectively. There are eleven 2D cases that cover the range of $U = 1$–$50\,\mathrm{m\,s}^{-1}$ with $5\,\mathrm{m\,s}^{-1}$ increments and four 3D cases that cover the range of $U = 10$–$40\,\mathrm{m\,s}^{-1}$ with $10\,\mathrm{m\,s}^{-1}$ increments. Table 1 summarizes the basic-flow and precipitation parameters, such as U, F_w, w_{oro} (orographic lifting), R_{max}, $X_{t\mathrm{max}}$ (location of maximum total rainfall), and $R_{t\mathrm{max}}$ for select 2D-Low and 2D-High, and all simulations in the 3D-LES setups.

Figure 3 shows the simulated distributions of 12-h accumulated rainfall for 2D-Low and 2D-High cases. The top large-domain plots clearly show that precipitation pattern is comparable within the wind speed range of 1–$30\,\mathrm{m\,s}^{-1}$. The bottom panels of Fig. 3 show a zoomed-in domain, which capture the finescale details of precipitation distribution. In this view, notable changes between 2D low- and high-resolution simulations are 1) the secondary precipitation maximum around $10\,\mathrm{m\,s}^{-1}$ is largest in 2D-Low; 2) precipitation structure changes for wind speeds above $20\,\mathrm{m\,s}^{-1}$ in 2D-Low, whereas precipitation amount increases linearly with wind in 2D-High simulations (right panels of Fig. 3); and 3) above $40\,\mathrm{m\,s}^{-1}$ both simulations show a localized precipitation maximum near the mountain peak with very heavy rainfall amounts. It is suspected that the 2D simulations or the model itself have reached their limits in producing realistic results under such high-wind stress, and thus we limit the wind speed scope at $40\,\mathrm{m\,s}^{-1}$.

The rainfall maxima that are obtained from 12-h accumulations and domain-integrated rainfall at 12 h versus the basic wind speed (Fig. 4) better shows the differences among simulation setups. The rainfall maxima, or the maximum points corresponding to the experiments, are obtained from the distributions of 12-h accumulated rainfall. The domain-integrated rainfall (right panel) is the accumulation of rainfall divided by 100 to get a reasonable number in the y axis. 2D-Low simulations are unable to capture precipitation peak (or at least the precipitation amount in the range of 30–$40\,\mathrm{m\,s}^{-1}$). Both 2D-High and 3D-LES simulations are in agreement in the 20–$40\,\mathrm{m\,s}^{-1}$ range. The relative change in precipitation intensity is larger when U is changed in $[30, 40]\,\mathrm{m\,s}^{-1}$ compared to that for $[20, 30]\,\mathrm{m\,s}^{-1}$ in both simulation setups. The physical processes associated with this behavior will be investigated in detail in the next section. Interestingly, the magnitude of precipitation is largest in 2D-Low when U is $10\,\mathrm{m\,s}^{-1}$. This can be explained by the fact that case U10 is very close to the regime II—a transitional regime between regimes I and III, as also revealed in Fig. 2, in which there is a force balance between the advection and density current (Chen and Lin 2005b). From the domain-integrated precipitation perspective, the trends are similar among the simulations, yet 2D-Low simulations produce smaller total precipitation at higher basic winds such as when $U > 20\,\mathrm{m\,s}^{-1}$.

MR09 stressed that 3D simulations are able to resolve precipitation more realistically. This is confirmed by looking at 10-h-averaged maximum updrafts and

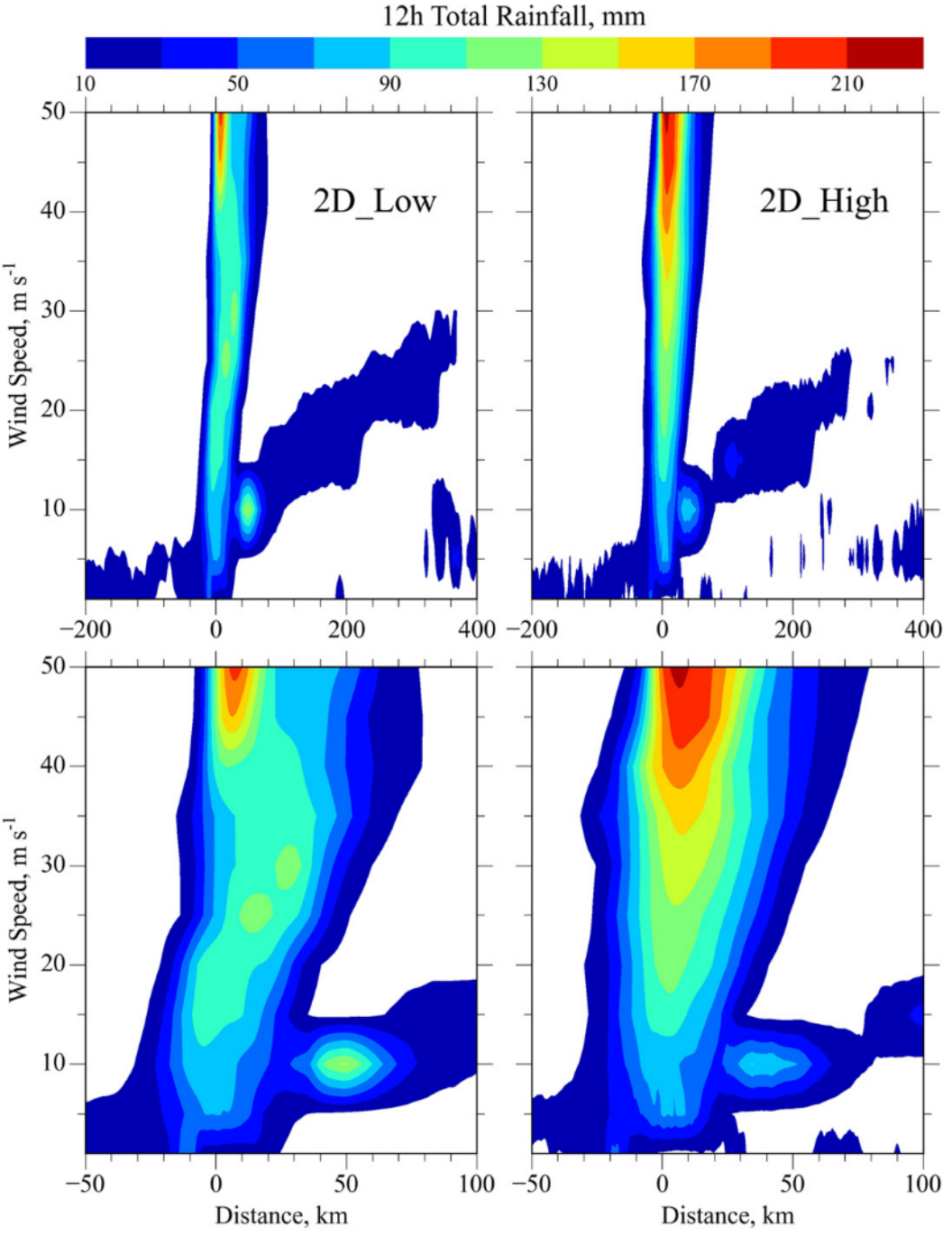

FIG. 3. Distributions of 12-h accumulated rainfall for (left) 2D low-resolution ($\Delta x = 1$ km, $\Delta z = 0.25$ km) and (right) 2D high-resolution ($\Delta x = 0.1$ km, $\Delta z = 0.1$ km) simulations. Parts of the simulated total domain are shown: (top) [−200, 400] and (bottom) [−50, 100] km.

downdrafts in each simulation (Fig. 5). These points are obtained by first finding the maxima and minima of updrafts/downdrafts in the whole domain and then averaging these values. We are interested in showing the convectively induced vertical motions, hence the order. This operation can be visualized also from Fig. 6 by averaging data points after 2 h. The maximum updrafts are nearly doubled in 3D-LES compared to those in 2D-Low. As mentioned in MR09, convection is a 3D phenomenon and 3D simulations provide a medium for the

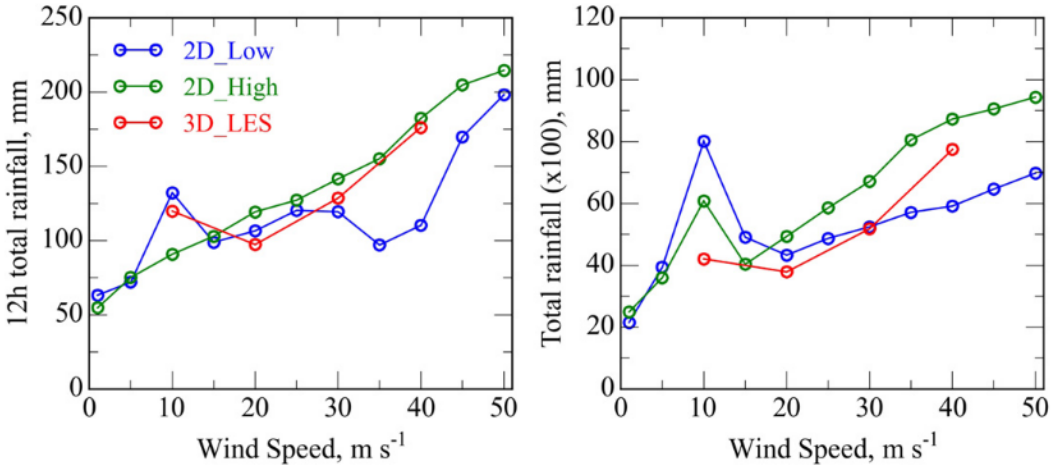

FIG. 4. (left) Total rainfall maxima which are obtained from 12-h accumulations for varying wind speeds and (right) domain-integrated rainfall.

updrafts and downdrafts to be established in both x and y dimensions. In 2D simulations, flow is confined in the x and z dimensions. Thus, strong updrafts and downdrafts cannot be represented as well as they are in 3D. Small-scale turbulent eddies cannot be resolved in a 2D-Low setup. Thus, convective cells and flow overturning are not captured realistically in low-resolution 2D simulations. In terms of downdrafts, the trend is more similar between 2D-High and 3D-LES, and both simulations capture the decrease of downdraft intensity reasonably in $U = 30$–$40\,\mathrm{m\,s^{-1}}$.

Time evolution of updrafts for 10 and $40\,\mathrm{m\,s^{-1}}$ cases are shown in Fig. 6. Data in these plots are based on 60-s outputs of maximum updraft in the whole domain. This plot highlights the turbulent nature of the simulations, particularly for the 3D setup, as the updrafts are not stationary in case U10. The updrafts are nearly doubled from $U = 10$ to $40\,\mathrm{m\,s^{-1}}$ in 2D-Low simulations, yet this change is smaller in the other setups. The variance of updrafts is larger in U40 compared to U10 for all of the simulation setups. This is expected, as the incoming flow has larger kinetic energy and microphysical processes are enhanced more at high wind speeds, resulting in strong updrafts and downdrafts. Another important difference between low- and high-resolution simulations is the timing of updraft response. Precipitation formation is delayed by 5–10 min in 2D-Low cases (see Fig. 6, 1 h into the simulation).

Figure 7 shows the horizontal distribution of 12-h total rainfall in a zoomed-in domain for cases U40 and U10. Here 3D-LES distributions are obtained by the y-averaged rain amount. The precipitation distribution

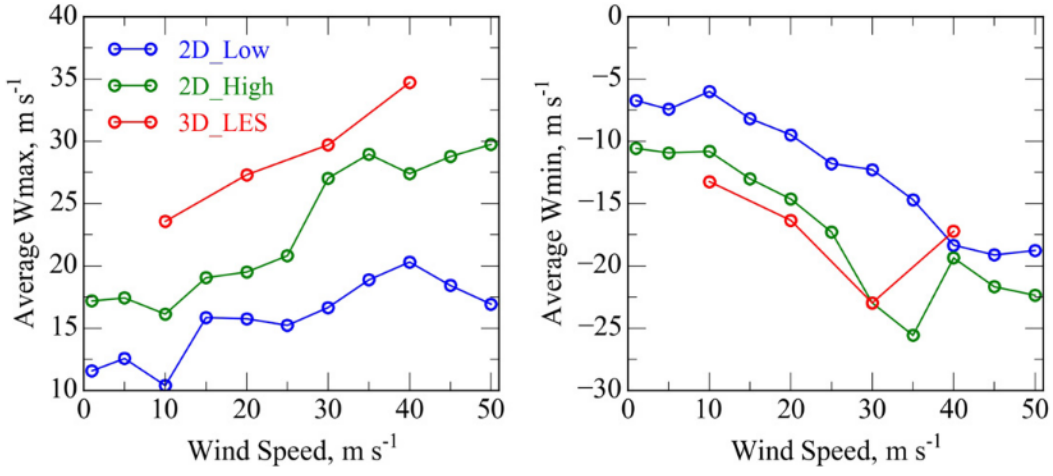

FIG. 5. Domain-averaged (between hours 2 and 12) (left) maximum and (right) minimum vertical velocities for varying wind speeds.

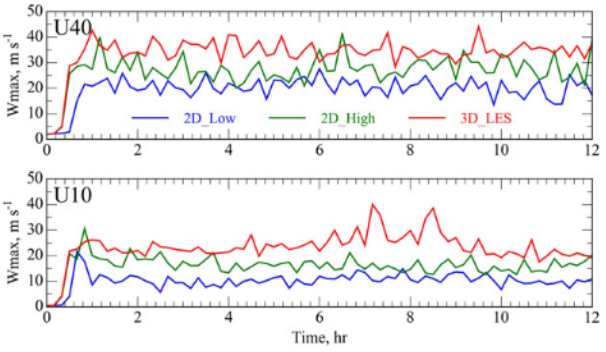

FIG. 6. Time series representation of maximum updraft velocity for (top) U40 and (bottom) U10.

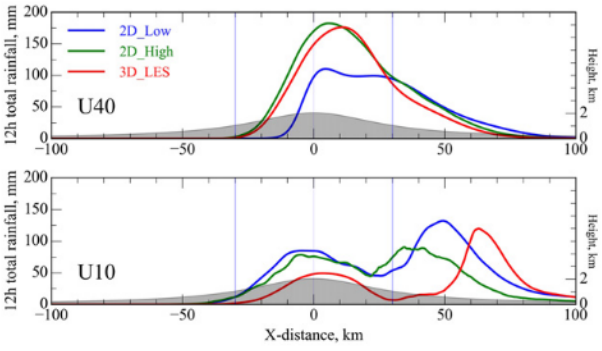

FIG. 7. Total rainfall distributions at 12 h for (top) U40 and (bottom) U10 over the domain [−100, 100] km.

described in U10 follows the early regime III characteristics, which show a stationary convective precipitation over the mountain along with a downstream moving component of the precipitation. In U10, 2D simulations produce larger precipitation over mountain as flow is restricted in y dimension. There are significant differences among the peak amount and peak location of precipitation for each case. These are transient features and precipitation is produced as a result of flow convergence at the leading edge of the hydraulic jump. Here, hydraulic jump refers to the downstream leading edge of severe downslope wind over the lee slope, which can be detected from the steepened isentropes (Smith 1985). A recent study by Nugent et al. (2014) shows that the basic-flow fields are similar in 2D and 3D Weather and Research Forecasting (WRF) Model simulations of a case similar to the U10 setup. However, they also note that the position and strength of hydraulic jump is sensitive to friction and critical-level height. In case U40, the precipitation amount and distribution are very similar for 2D-High and 3D-LES. This is expected at higher wind speeds since the incoming flow can climb over the mountain easily and the impact of transient features diminish.

To get better insight into the precipitation differences among the simulated cases, model fields at 3 and 12 h are provided in Fig. 8 within the horizontal domain of −50–80 km. The largest precipitation maxima noted in 2D-Low in Fig. 7 (bottom) is produced by strong updraft cells forming slightly downslope of the mountain. The 2D-Low setup nearly misses the downdrafts that are apparent in 2D-High and 3D-LES cases, downstream of the mountain ahead of the strong-updraft region. Compared to 2D-High, 2D-Low cases have stronger winds near the surface and aloft, over the downslope of the mountain, which contributes to further advection of precipitation. Flow fields are comparable at 3 h for 2D-High and 3D-LES (third row, y centered), yet significant differences emerge at 12 h, particularly the location of hydraulic jump, magnitude of flow acceleration downslope of the mountain, and the organization vertical motion fields. A hydraulic jump is able to form at about $x = 50$ km in 3D flows, yet is not completely formed in the 2D-Low case, while more pronounced in the 2D-High simulation. The isentropes are much steepened in 3D-LES, the jump is well organized downslope, and highly turbulent mixed region behind the jump is seen from the weak winds. However, the y-averaged fields (bottom panel) illustrate the wave breaking and hydraulic jump structures more visibly as small-scale perturbation are filtered in this view. Since the convection cells could develop in each direction rather than being restricted to solely (x, z) dimensions, the fields in 3D are well organized as a result of stationary 2D mechanical (orographic) forcing. Strong winds near the surface as well as a more structured hydraulic jump formation in 3D explain the farthest downstream advection of heavy precipitation among the U10 cases.

Although 2D-Low simulations are able to capture orographic precipitation and flow fields reasonably well, 3D-High simulations are required to capture turbulent and microphysical processes and their interactions at high winds.

5. Evolution of precipitating system at higher winds

a. General precipitation characteristics

In this section, the dynamical and physical processes that modulate orographic precipitation intensity and distribution at high wind speeds (i.e., $U = 20$, 30, and 40 m s^{-1}) are analyzed using the outputs from the 3D-LES setup. Low-wind regimes for a conditionally unstable, vertically uniform flow over a mesoscale mountain are well studied in CL00 and MR09 with idealized simulations. Here, we expand the analysis of orographic precipitation to much higher wind speeds, such as those

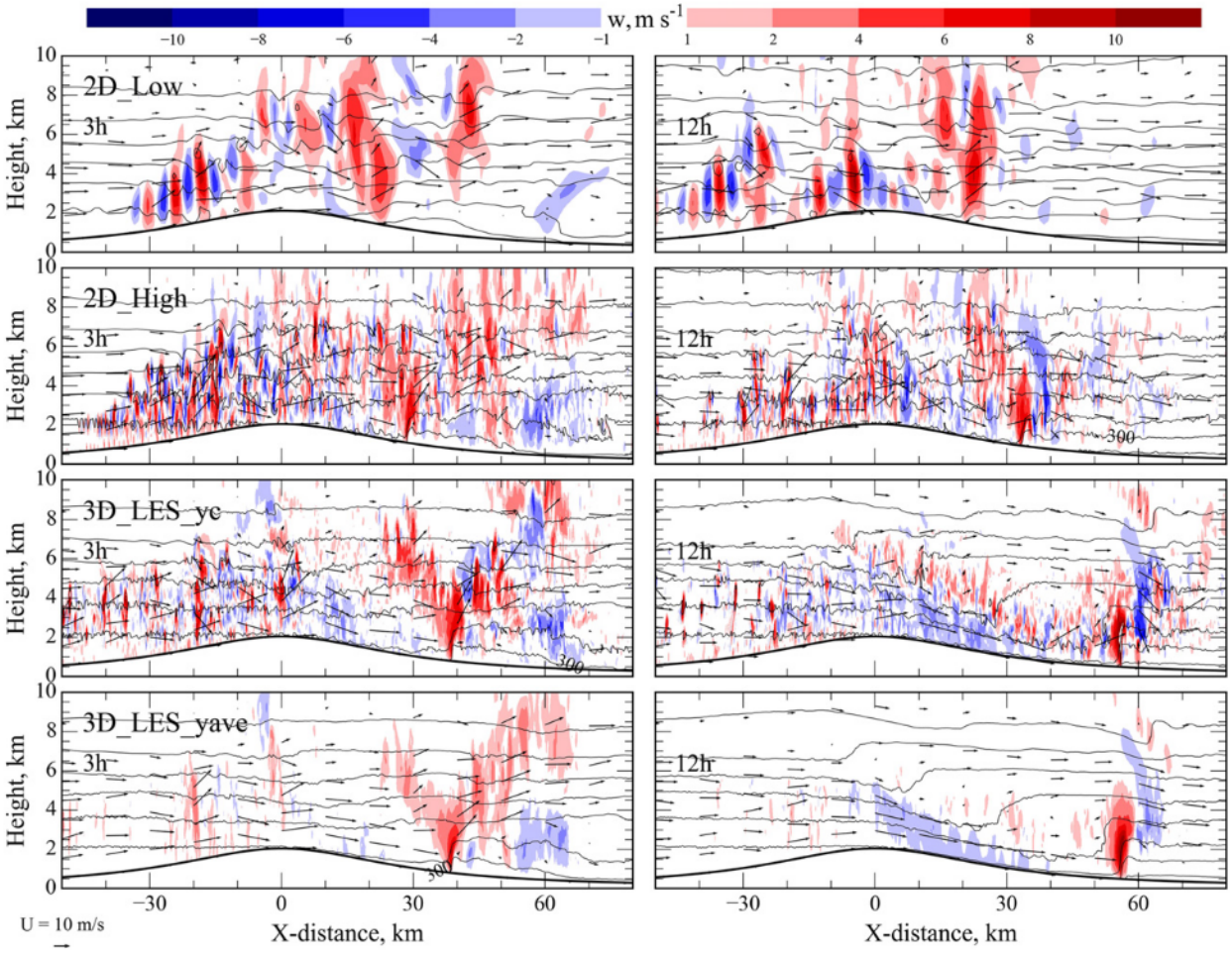

FIG. 8. Evolutions of the potential temperature (thin line contours plotted at every 5 K), vertical velocity (filled contours in the range from −12 to 12 m s^{-1} with red indicating updraft and blue indicating downdraft regions), and wind vector fields at (left) 3 and (right) 12 h for U10. Simulation types are identified in the left column and 3D-LES-yc fields are plotted at the center of the *y* domain; 3D-LES-yave fields are *y*-domain-averaged values. Plotting domain is zoomed in to 10 km vertically and [−50, 80] km horizontally.

occurring in TC environments. Presence of high-wind dry environments is conducive to various natural hazards, such as downslope windstorms and clear-air turbulence when flow passes over terrain. However, inclusion of moisture, conditional instability, and orography make forecasting even more challenging with increased complexity of precipitation processes.

We start by evaluating the distribution of rainfall in three high-wind cases simulated in 3D-LES setting. These cases are illustrated in Fig. 9. The top panels of this plot show the time evolution of rain rate within −50–500 km of the domain. Cases U20 and U30 are still in the range of regime III with their stationary precipitation component near the mountain and followed by downstream-propagating branches. Note the magnitude of precipitation increases near the mountain and decreases in downstream branch, which is linked with the increase in U as a result of increased updrafts and rapid flow advection. The advection speed of the downstream branch can be estimated from the horizontal location of the rain rate. This transient precipitating system propagates downstream at 30 and 60 m s^{-1} for cases U20 and U30, respectively. This speed difference highlights the rapid flow acceleration at U30 compared to U20. When the system is pushed to 40 m s^{-1}, the downstream system propagates out of the domain at 12 h and precipitation accumulates near the mountain. Based on this particular behavior of precipitation and later analyses of flow fields, this moist flow regime is classified as regime IV at U40.

In the bottom panels of Fig. 9, the zoomed-in rainfall distribution is overlaid with 12-h total precipitation. This plot shows that the rainfall rate increases with wind speed. The location of precipitation

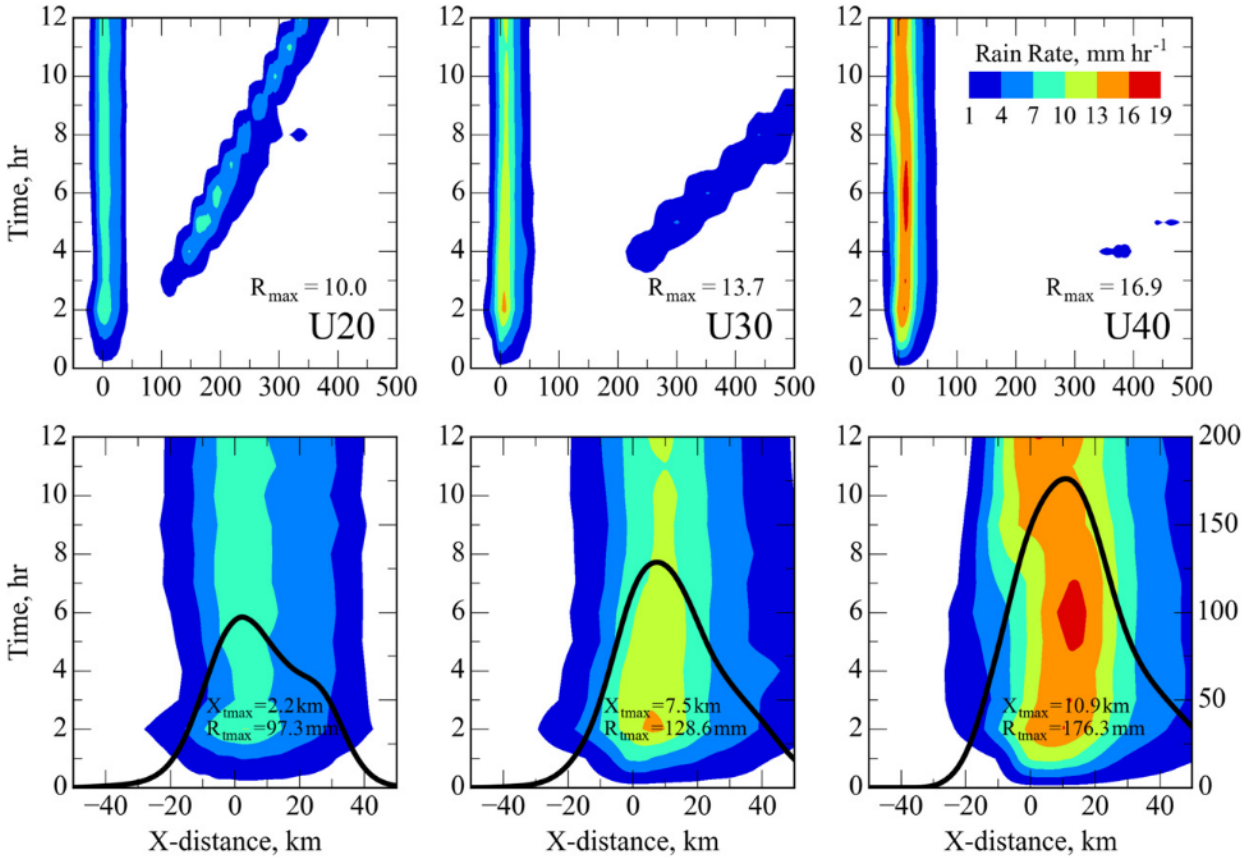

FIG. 9. Hovmöller representation of rain rate for (left) U20, (center) U30, and (right) U40 based on 3D-LES over the domain of (top) [−50, 500] and (bottom) [−50, 50] km. The black line in the bottom panels shows the distribution of 12-h accumulated precipitation. Basic precipitation statistics, such as maximum rain rate R_{max}, maximum total rain R_{tmax}, and the location of maximum total rain X_{tmax} are provided in the panels.

maximum shifts downstream (by about 5 km) with increasing wind speed as spillover effect increases. Additionally, weak secondary precipitation maximum diminishes as the downstream branch weakens at higher winds. The total accumulated rain for 12 h increases much more (~50 mm) when U increases from U30 to U40, compared to that (~30 mm) from U20 to U30.

b. *Evolutions of the convective system and orographic precipitation*

Figure 10 shows the structural evolutions of the precipitating system at 3 and 12 h, such as along-ridge (y)-averaged flow fields, potential temperature, vertical velocity, and cloud fields. Since these fields result from 100-m-grid-resolution simulations, some smoothing (using a Gaussian filter function) is applied to reveal the overall flow evolutions, which reduces the vertical velocities. However, the increasing trend in the updraft strength can still be seen from the U20 to U40 cases, as orographic lifting (i.e., $\sim U\partial h/\partial x$) increases at higher wind speeds and convectively driven updrafts are strengthened.

Both cases U20 and U30 show a distinct structure of hydraulic jump formation at 12-h plots. The downdrafts are focused on the downslope of the mountain and gravity wave–induced cloud formation is visible over the lee slope. Among the cases, it is also noticeable that the strongest downdrafts are produced in U30 associated with deep upper-level wave breaking. The tightly packed isentropes are evidence of strong flow acceleration downstream of the mountain, indicating the occurrence of a severe downslope wind event. In case U40, this upper-level wave breaking and its associated hydraulic jump disappears as the flow transitions to an evanescent flow regime (i.e., vertically propagating gravity waves fade away exponentially).

Evolution of hydrometeors (rain, snow, graupel), wind, and turbulent kinetic energy (TKE) fields are presented in Fig. 11. Note that in order to get a clear view, the snow, graupel, and turbulence fields are smoothed. At 3 h, the convective cells overall deepen

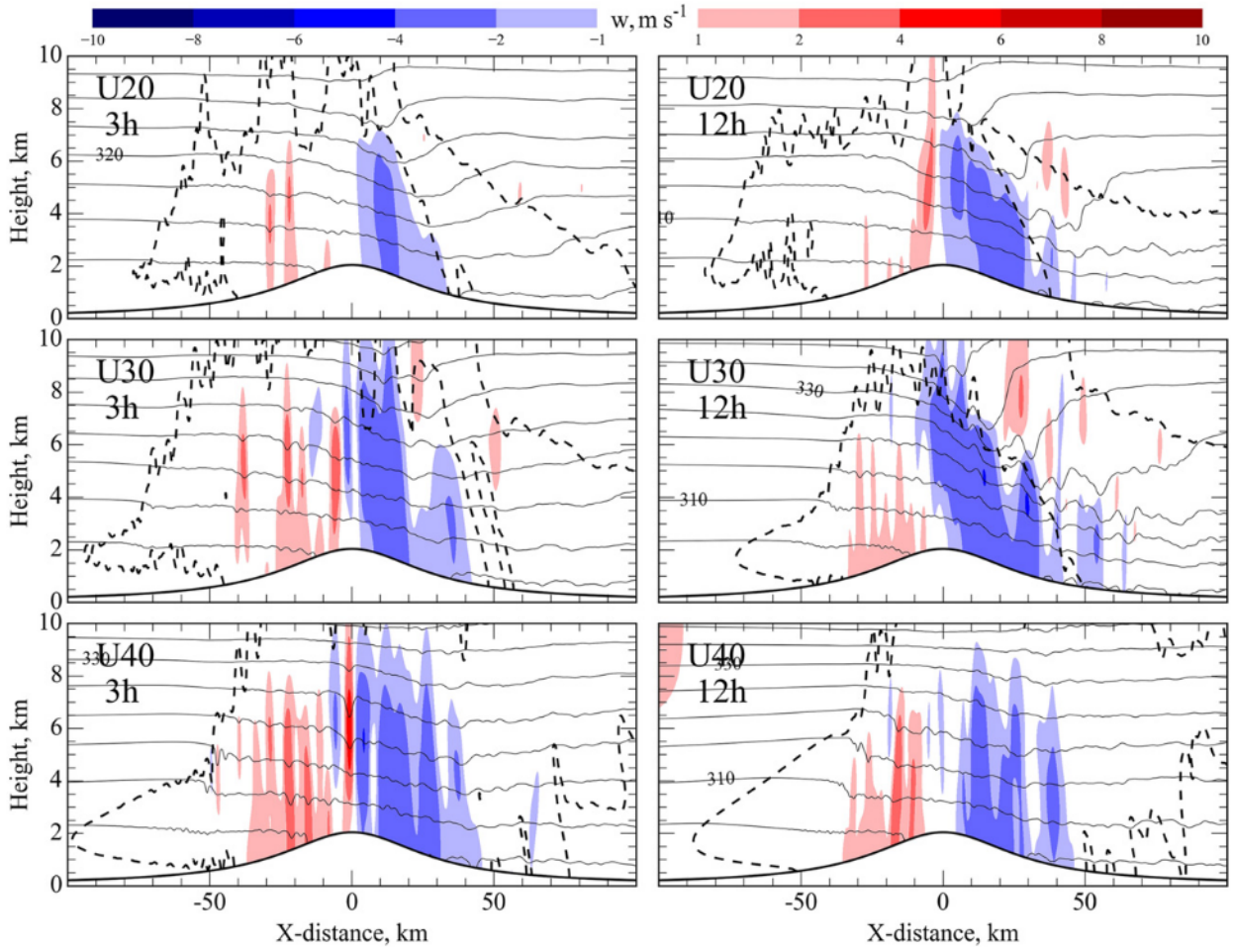

FIG. 10. Evolutions of the along-ridge (y)-averaged potential temperature (thin line contours plotted at every 5 K), vertical velocity (filled contours in the range from -10 to 10 m s^{-1} with red indicating updraft and blue indicating downdraft regions), cloud envelope (thick dashed line contoured for the combined hydrometeor values that are greater than 0.1 g kg^{-1}) at (left) 3 and (right) 12 h for (top) U20, (middle) U30, and (bottom) U40. Plotting domain is zoomed in to 10 km vertically and [−100, 100] km horizontally.

proportionally to the basic wind speed. This deepening is mainly caused by the orographic forcing, which can be roughly represented by $w_{oro} \approx U\partial h/\partial x$ (e.g., Lin et al. 2001), and can be seen clearly at 3 h in U20 and U30. The deeper vertical development of the convective cells over the lee slope from U30 to U40 is partially due to the faster wind near the surface and partially due to the increase of vertical wavelength. This, in turn, enhances graupel and snow formation, as can be seen clearly from the U30 and U40 panels. These effects are most noticeable in U30, as the largest low-level flow acceleration is observed in this case. At 3 h, turbulence signal, as measured by the TKE, is only present in the region of convective activity associated with buoyancy.

At 12 h of U20 and U30, as the wave breaking matures, the turbulence becomes apparent over the lee slope in middle to upper troposphere and downstream of the mountain. In U30, as the gravity waves amplify, more TKE are generated downstream of the mountain leading to hydraulic jump with turbulence mixing and a dead region (Smith 1985), which can be seen clearly from the wind field (right-middle panel of Fig. 11). Strong turbulence is mechanically produced in this region which is associated with flow-induced wind shear. For U40, this region of strong shear and turbulence mixing vanishes as the wave breaking disappears when the upward-propagating waves are no longer supported. That is, the system transitions to the evanescent flow regime at this high flow speed, when $l_w < k$ as shown in Eq. (3b). In U20 and U30, the convective cells over the lee slope are limited vertically by the upper-level wave breaking and turbulence mixing associated with the hydraulic jump, leading to the shallower convective cells and lighter and narrower precipitation downstream of the mountain as well as the ice-phase production of

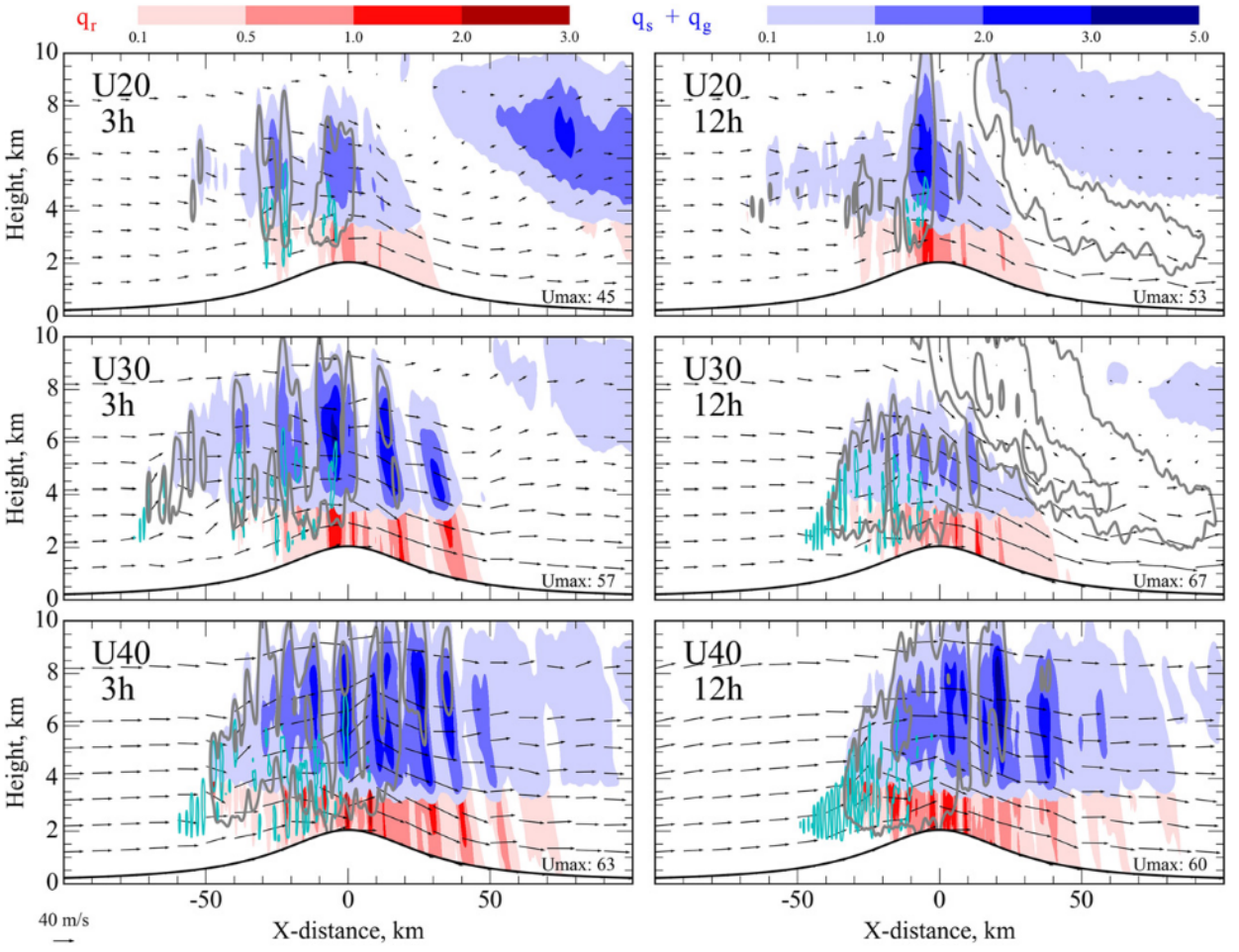

FIG. 11. Evolutions of the along-ridge (y)-averaged warm (q_r; red-filled contours between 0.1 and 3 g kg^{-1}) and cold ($q_s + q_g$; blue-filled contours between 0.1 and 5 g kg^{-1}) hydrometeors and wind vector fields. Cyan line contours show cloud water mixing ratio greater than 1 g kg^{-1} at (left) 3 and (right) 12 h for (top) U20, (middle) U30, and (bottom) U40. Gray line contours show TKE within 1–10 m^2 s^{-2} at five intervals. Plotting domain is zoomed in to 10 km vertically and [−100, 100] km horizontally. Maximum surface velocities U_{max} (m s^{-1}) are included in each panel.

rainfall. Once the system transitions to the new flow regime and buoyant production of turbulence is intensified, rainfall production is enhanced. Although cell growth is limited in U20 and U30 cases, once the hydraulic jump formation matures at 12 h, surface winds can more than double in strength downstream of the mountain. Note that the strongest cell formed over the mountain peak in U20 (12 h) is likely due to the position of the upper-level wave. In this case, the hydraulic jump occurs near the surface and farther downwind, and thus convective cells are partially blocked over the mountain. A deeper cell formation right over the mountain peak might be attributed to the favored position of wave-breaking region, which is limiting the cell growth downwind of the mountain.

A top-down view of vertical velocity and TKE fields at a height of 5 km for 12-h outputs are presented in Fig. 12 to illustrate the zonal and meridional variability. Even though the flow is symmetrical in the y direction and an infinitely long 2D ridge is used, asymmetrical flow features emerge in the domain, as conditional instability is trigged by orographic forcing. These asymmetrical features cannot be simulated in 2D simulations owing to the limitations of domain geometry. In terms of wind speed variation, the largest updrafts regions are formed at U40 as a result of strong orographic lifting. Yet, some of these convective updrafts are compensated by large downdrafts. Updrafts are shifted significantly leeward when U is increased. Again, this can be a result of strong flow advection. The TKE fields clearly show the regions of heavy shear associated with wave breaking and hydraulic jump, 30–40 km downwind of the mountain at U20 and U30. When the wind speed is increased, buoyancy production term increases, therefore TKE responses positively upwind of the mountain. Since

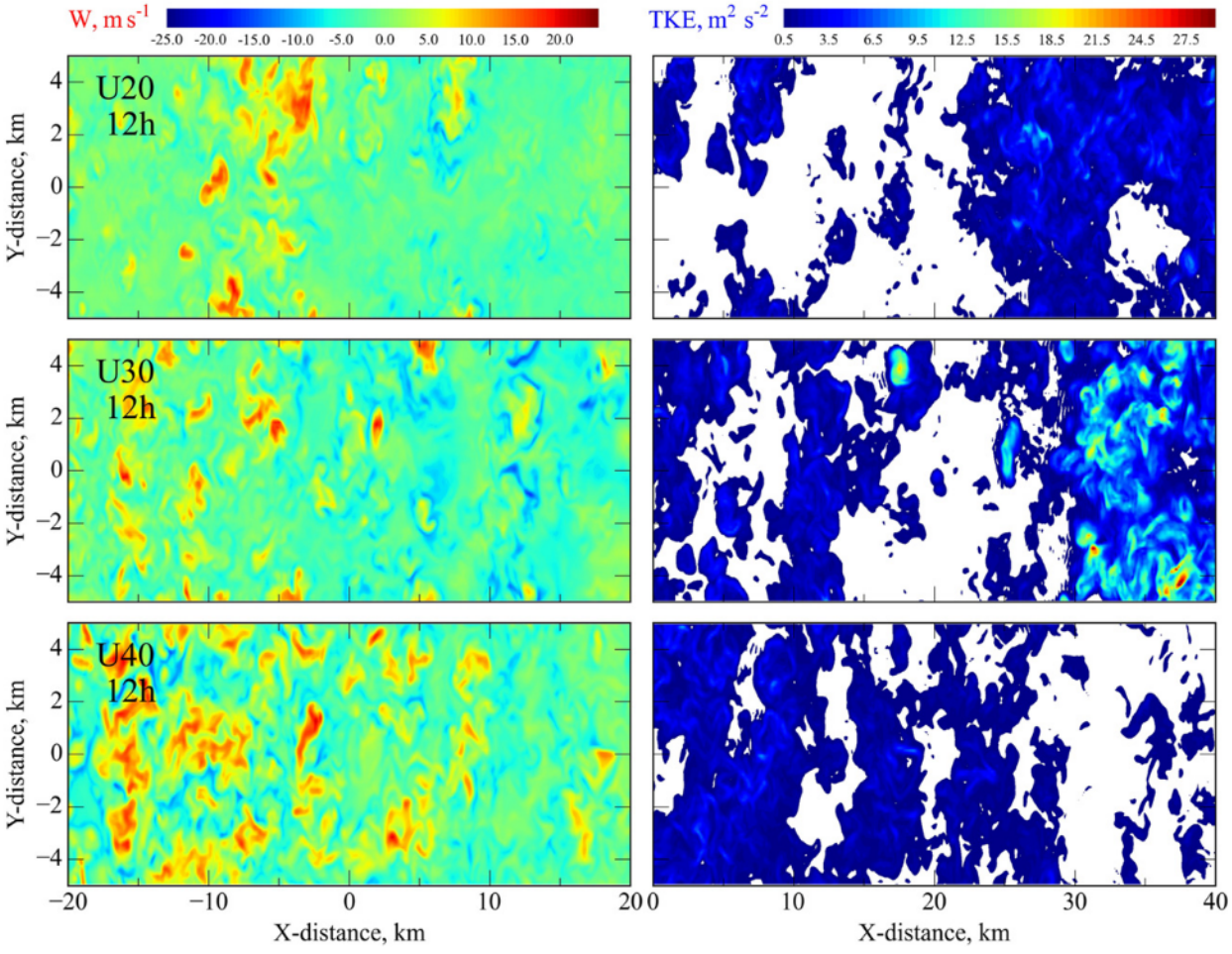

FIG. 12. Simulated 12-h (left) vertical velocity fields (m s^{-1}) in the horizontal domain [−20, 20] km × [−5, 5] km and (right) TKE fields (m^2 s^{-2}) in the horizontal domain of [0, 40] km × [−5, 5] km at z = 5 km for (top) U20, (middle) U30, and (bottom) U40 cases.

the system transitions to evanescent flow regime at U40, TKE response is almost negligible at 30–40 km of domain.

Figure 13 shows the along-ridge-averaged horizontal distributions of maximum and minimum vertical velocities (top) and vertically averaged hydrometeors (middle) at 12 h. Overall, the updraft magnitude and frequency increases as U increased. The downdraft magnitude also increases upwind of the mountain. Yet U30 shows the largest velocities downwind of the mountain as a result of severe downslope wind. Except at the local peak of U20, all hydrometeor content increases with increasing basic wind speeds. As explained above, the formation of lower hydraulic jump that is associated with lower critical level (Lin 2007) provides blocking of the convective cells over the peak. The local maximum is clearly linked with the localized updrafts. However, there are no clear updraft–hydrometeor relations in these plots. Location of hydrometeor peaks shifts farther to the right owing to intensified advection velocities at U40.

Local maxima of rain are collocated with those of snow and graupel, implying the important roles played by the ice phase microphysical processes. Validation of this claim requires a microphysics budget analysis (Colle and Zeng 2004; Yang et al. 2011) to determine dominant precipitation production and sink terms. The warm base nature of the input sounding would restrict the surface precipitation to rain only. This would simplify the budget analysis to only rain source and sink terms. An initial assessment of rain budget indicates that autoconversion of cloud water and accretion of cloud water by raindrops are other dominant processes for rainfall production. This finding is logically expected, owing to the warm low-level temperatures (~15°C) and near-4-km freezing level specified in the initial idealized sounding.

Time-averaged rain mixing ratio distribution (Fig. 13) clearly shows the pattern of rainfall (Fig. 9). The impact

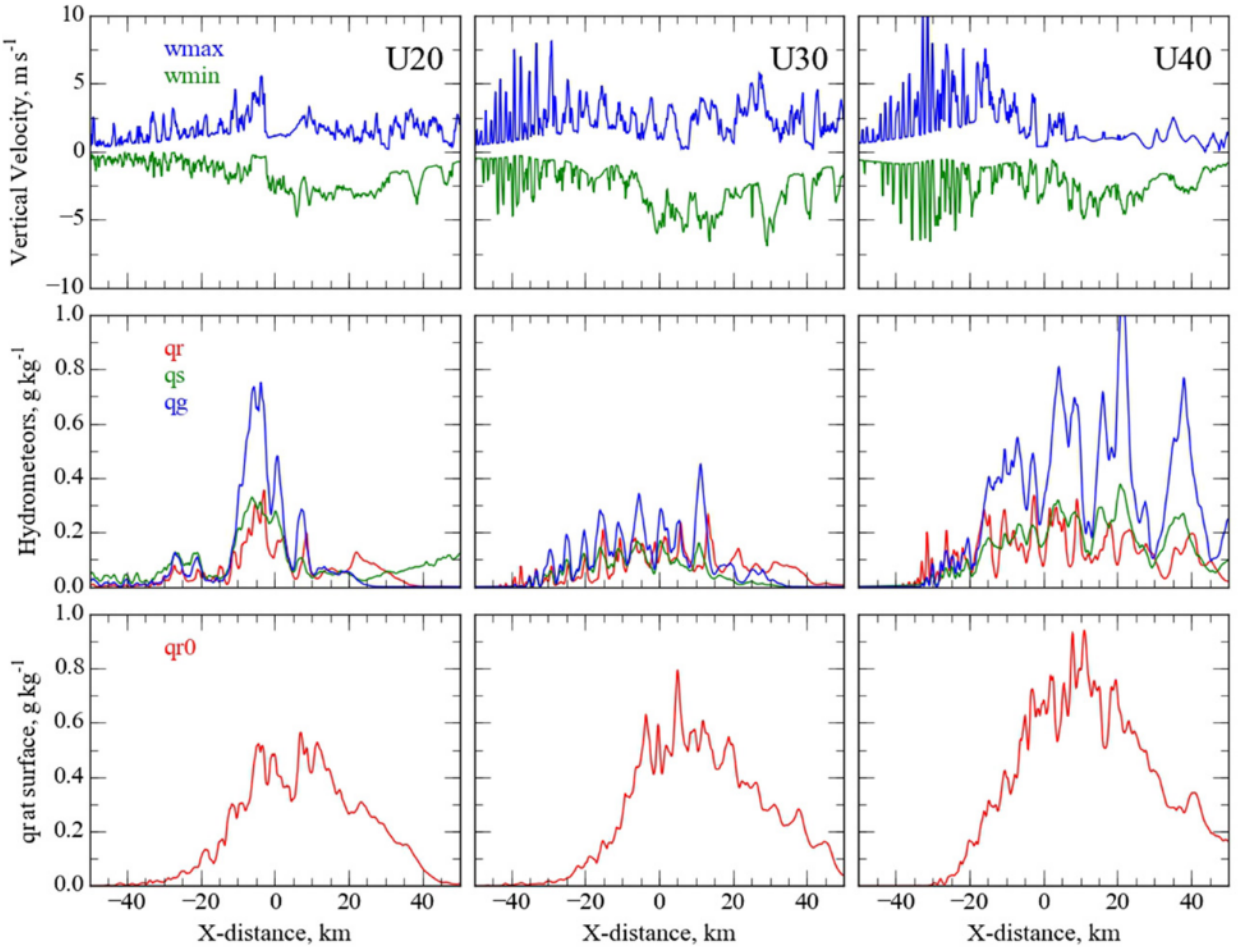

FIG. 13. (top) Maximum and minimum vertical velocities; (middle) vertically averaged rain, snow, and graupel mixing ratio distributions at 12 h, and (bottom) surface fields of rain mixing ratio distribution, which are averaged over the entire simulation for (left) U20, (center) U30, and (right) U40. The highly varying flow fields can be seen in this zoomed-in horizontal domain of [−50, 50] km.

of snow and graupel melting play a role in the precipitation difference between cases. As flow transition to the evanescent regime at U40, all precipitating hydrometeors are enhanced, yet the amount of intensification in surface rainfall is not as strong. This discrepancy may be attributed to enhanced evaporation and sublimation with increasing wind speed, which limits rain reaching the surface. Additionally, enhanced horizontal transport of ice hydrometeors by strong advection might explain the disproportional enhancement in rainfall. However, detailed dynamics and microphysics interactions need to be further studied to explain the partitioning of water vapor in this high-wind orographic precipitation system.

6. Concluding remarks

Two- and three-dimensional idealized simulations of conditionally unstable, uniform basic flow over a fixed-height bell-shaped mountain have been investigated using CM1. We were able to reproduce CL00's findings qualitatively using the low-resolution 2D simulations, although the details of each flow regime differ as a result of model numerics and setup. Regime I is characterized by a stationary convective precipitation over the mountain with an upstream-propagating density current and convective system. Regime II is characterized by heavy convective precipitation focused in the vicinity of the mountain peak. This regime might produce heavy local rainfall near the mountain if it persists over a long period, potentially leading to flash floods. Regime III is characterized by a convective cloud system remaining stationary near the mountain and a downstream moving convective system. Regime IV occurs when U is further increased to 36 m s^{-1} and above and is characterized with a stationary convective precipitating system near the mountain peak and heavy precipitation over the lee slope. This regime is similar to regime III, but with distinct dynamical changes in the flow structure with the

lack of large upper-level wave breaking, middle-level hydraulic jump, and lower-level flow acceleration over the lee slope. Note that the flow structures of high winds (e.g., $U > 25\,\mathrm{m\,s^{-1}}$) and the regime transition at regime IV were not studied in CL00.

Even though the flow dynamics are captured in 2D low resolution for both low- and high-wind-speed simulations, distinct differences are noted in vertical velocity, turbulence, and, more importantly, precipitation characteristics in high-resolution 2D and 3D simulations. Most notable of these differences is that 2D-Low simulations represent orographic precipitation distribution and intensity reasonably when wind speeds are less than about $30\,\mathrm{m\,s^{-1}}$. Based on the analysis of the intensity and distribution of updrafts and downdrafts, only high-resolution 3D simulations are shown to represent the true nature of convection development. The difference in orographic precipitation distribution between low- and high-resolution simulations may be attributed to the inefficiency of moist and turbulent parameterization schemes while resolving dynamical and physical process interactions at high wind speeds. Given the highly unstable sounding and infinitely long mountain ridge, we expect to see some variation in these conclusions. We plan to investigate the impact of instability associated with varying CAPE on the resolution and dimensionality in a separate study.

Dynamical and physical evolution of flow structure is further analyzed using 3D high-resolution-based high-wind-speed simulations. The orographic precipitation is increased more when U is increased from 30 to $40\,\mathrm{m\,s^{-1}}$ compared to that from 20 to $30\,\mathrm{m\,s^{-1}}$ because of the disappearance of hydraulic jump with turbulence mixing region over the lee slope when the system transitions to regime IV. In addition, the distribution of orographic precipitation become more uniform for $U = 40\,\mathrm{m\,s^{-1}}$ compared to the double peak patterns simulated in cases with $U = 20$ and $30\,\mathrm{m\,s^{-1}}$. These behaviors are explained by the change in upper-level flow structure when the basic wind speed exceeds the critical speed of $U = 36\,\mathrm{m\,s^{-1}}$. The transition from regime III to regime IV at $36\,\mathrm{m\,s^{-1}}$ can be explained by the transition from upward-propagating gravity waves to evanescent flow, which can be predicted by an existing mountain wave theory with the Scorer's equation. In this treatment, upstream profiles of the atmosphere are sufficient to depict the flow transition without considering the effect of convection and precipitation near the mountain. Strong turbulence mixing noted in regime III is associated with large upper-level wave breaking and wave overturning. Although this flow behavior has little impact on precipitation amount, surface wind intensity is more than doubled downstream of the mountain, resulting in a severe downslope windstorm. In regime IV, this additional flow acceleration ceases, which allows the convective cells to develop into upper troposphere leading to larger graupel and snow production. Additionally, a preliminary simple rain budget analysis, which will be explored further in a separate paper, indicates that enhanced warm-rain autoconversion and accretion processes as well as the aforementioned ice-phase rain sources contribute more significantly when the blocking effect of wave breaking vanishes. However, evaporation and sublimation processes within strong convective downdrafts limits the enhancement of surface rainfall.

A plausible extension of this idealized study would be to simulate more realistic atmospheric conditions (e.g., one that is more representative of TC environment in terms of moisture and vertical wind speed profiles). In addition, adaptation of a realistic terrain profile would enhance the applicability of these results to real-world conditions. It should be reminded that reproduction of these results are strongly dependent on the numerical model employed, model version, initial sounding, dimensionality (2D and 3D), as well as dynamics and physics options. However, the overall conclusions should remain similar in varying environments, if not the exact quantitative findings. Transient features such as wave breaking and hydraulic jump formation processes, particularly at high-wind speeds, are highly sensitive to the model boundary conditions. Simulations with a PBL scheme yield a similar precipitation distribution and reduced intensity compared to the highly idealized free-slip simulations, a finding similar to that of Chiao et al. (2004). The impacts of friction and PBL on flow behavior and precipitation are very complicated, and are beyond the scope of this study, thus deserving further investigation. However, the present study is a first step before exploring more complicated processes associated with high-wind-speed, moist flow over mountains.

Acknowledgments. Discussion with Dr. Richard Rotunno, proofreading by Megan L. Jordano, and comments made by the anonymous reviewers are highly appreciated. This research was supported by the National Science Foundation Awards AGS-1265783, HRD-1036563, OCI-1126543, and CNS-1429464.

REFERENCES

Baines, P. G., 1995: *Topographic Effects in Stratified Flow*. Cambridge University Press, 482 pp.

Barcilon, A., J. C. Jusem, and P. G. Drazin, 1979: On the two-dimensional, hydrostatic flow of a stream of moist air over a mountain ridge. *Geophys. Astrophys. Fluid Dyn.*, **12**, 125–140, doi:10.1080/03091927908243765.

Bryan, G. H., and J. M. Fritsch, 2002: A benchmark simulation for moist nonhydrostatic numerical models. *Mon. Wea. Rev.*, **130**, 2917–2928, doi:10.1175/1520-0493(2002)130<2917:ABSFMN>2.0.CO;2.

Chen, S.-H., and Y.-L. Lin, 2005a: Orographic effects on a conditionally unstable flow over an idealized three-dimensional mesoscale mountain. *Meteor. Atmos. Phys.*, **88**, 1–21, doi:10.1007/s00703-003-0047-6.

——, and ——, 2005b: Effects of moist Froude number and CAPE on a conditionally unstable flow over a mesoscale mountain ridge. *J. Atmos. Sci.*, **62**, 331–350, doi:10.1175/JAS-3380.1.

——, ——, and Z. Zhao, 2008: Effects of unsaturated moist Froude number and orographic aspect ratio on a conditionally unstable flow over a mesoscale mountain. *J. Meteor. Soc. Japan*, **86**, 353–367, doi:10.2151/jmsj.86.353.

Chiao, S., Y.-L. Lin, and M. L. Kaplan, 2004: Numerical study of the orographic forcing of heavy precipitation during MAP IOP-2B. *Mon. Wea. Rev.*, **132**, 2184–2203, doi:10.1175/1520-0493(2004)132<2184:NSOTOF>2.0.CO;2.

Chu, C.-M., and Y.-L. Lin, 2000: Effects of orography on the generation and propagation of mesoscale convective systems in a two-dimensional conditionally unstable flow. *J. Atmos. Sci.*, **57**, 3817–3837, doi:10.1175/1520-0469(2001)057<3817:EOOOTG>2.0.CO;2.

Colle, B. A., 2004: Sensitivity of orographic precipitation to changing ambient conditions and terrain geometries: An idealized modeling perspective. *J. Atmos. Sci.*, **61**, 588–606, doi:10.1175/1520-0469(2004)061<0588:SOOPTC>2.0.CO;2.

——, and Y. Zeng, 2004: Bulk microphysical sensitivities within the MM5 for orographic precipitation. Part I: The Sierra 1986 event. *Mon. Wea. Rev.*, **132**, 2780–2801, doi:10.1175/MWR2821.1.

Houze, R. A., Jr., 2012: Orographic effects on precipitating clouds. *Rev. Geophys.*, **50**, RG1001, doi:10.1029/2011RG000365.

Huang, Y.-C., and Y.-L. Lin, 2014: A study on the structure and precipitation of Morakot (2009) induced by the Central Mountain Range of Taiwan. *Meteor. Atmos. Phys.*, **123**, 115–141, doi:10.1007/s00703-013-0290-4.

Lin, Y.-L., 2007: *Mesoscale Dynamics.* Cambridge University Press, 630 pp.

——, and T.-A. Wang, 1996: Flow regimes and transient dynamics of two- dimensional stratified flow over an isolated mountain ridge. *J. Atmos. Sci.*, **53**, 139–158, doi:10.1175/1520-0469(1996)053<0139:FRATDO>2.0.CO;2.

——, R. D. Farley, and H. D. Orville, 1983: Bulk parameterization of the snow field in a cloud model. *J. Climate Appl. Meteor.*, **22**, 1065–1092, doi:10.1175/1520-0450(1983)022<1065:BPOTSF>2.0.CO;2.

——, S. Chiao, T.-A. Wang, and M. L. Kaplan, 2001: Some common ingredients for heavy orographic rainfall. *Wea. Forecasting*, **16**, 633–660, doi:10.1175/1520-0434(2001)016<0633:SCIFHO>2.0.CO;2.

Miglietta, M. M., and R. Rotunno, 2009: Numerical simulations of conditionally unstable flows over a mountain ridge. *J. Atmos. Sci.*, **66**, 1865–1885, doi:10.1175/2009JAS2902.1.

——, and ——, 2010: Numerical simulations of low-CAPE flows over a mountain ridge. *J. Atmos. Sci.*, **67**, 2391–2401, doi:10.1175/2010JAS3378.1.

——, and ——, 2014: Numerical simulations of sheared conditionally unstable flows over a mountain ridge. *J. Atmos. Sci.*, **71**, 1747–1762, doi:10.1175/JAS-D-13-0297.1.

Nugent, A. D., R. B. Smith, and J. R. Minder, 2014: Wind speed control of tropical orographic convection. *J. Atmos. Sci.*, **71**, 2695–2712, doi:10.1175/JAS-D-13-0399.1.

Schalkwijk, J., H. J. J. Jonker, A. P. Siebesma, and E. Van Meijgaard, 2015: Weather forecasting using GPU-based large-eddy simulations. *Bull. Amer. Meteor. Soc.*, **96**, 715–723, doi:10.1175/BAMS-D-14-00114.1.

Smith, R. B., 1979: The influence of mountains on the atmosphere. *Advances in Geophysics*, Vol. 21, Academic Press, 87–230, doi:10.1016/S0065-2687(08)60262-9.

——, 1985: On severe downslope winds. *J. Atmos. Sci.*, **42**, 2597–2603, doi:10.1175/1520-0469(1985)042<2597:OSDW>2.0.CO;2.

Sun, W.-Y., and O. M. Sun, 2015: Bernoulli equation and flow over a mountain. *Geosci. Lett.*, **2**, 7, doi:10.1186/s40562-015-0024-1.

Tao, W.-K., and J. Simpson, 1993: Goddard Cumulus Ensemble Model. Part I: Model description. *Terr. Atmos. Oceanic Sci.*, **4**, 35–72.

Weisman, M. L., and J. B. Klemp, 1982: The dependence of numerically simulated convective storms on vertical wind shear and buoyancy. *Mon. Wea. Rev.*, **110**, 504–520, doi:10.1175/1520-0493(1982)110<0504:TDONSC>2.0.CO;2.

Xue, M., K. K. Droegemeier, and V. Wong, 2000: The Advanced Regional Prediction System (ARPS)—A multi-scale nonhydrostatic atmospheric simulation and prediction tool. Part I: Model dynamics and verification. *Meteor. Atmos. Phys.*, **75**, 161–193, doi:10.1007/s007030070003.

Yang, M.-J., S. A. Braun, and D.-S. Chen, 2011: Water budget of Typhoon Nari (2001). *Mon. Wea. Rev.*, **139**, 3809–3828, doi:10.1175/MWR-D-10-05090.1.